Preprints of the 21st IFAC World Congress (Virtual)
Berlin, Germany, July 12-17, 2020

Design of parallel compensator and stabilizing controller to mitigate non-minimum phase behaviour of the Czochralski Process

Halima Zahra Bukhari * **Morten Hovd** *
Muhammad Faisal Aftab ** **Jan Winkler** ***

* *Department of Engineering Cybernetics, NTNU, Trondheim, Norway (e-mail: halima.bukhari@ntnu.no; morten.hovd@ntnu.no).*
** *Department of Engineering Sciences, University of Agder, Norway*
*** *Institute of Control Theory, Faculty of Electrical & Computer Engineering, TU Dresden, Germany, (e-mail: jan.winkler@tu-dresden.de)*

Abstract: This paper addresses the design of a parallel compensator and a stabilizing controller for the simplified crystal growth dynamics of the Czochralski (CZ) process, i.e., the process for the production of monocrystalline silicon ingots of uniform diameter. The diameter control of the produced ingots is achieved by a CCD camera measurement used to sense the radius of the boundary between the base of the growing crystal and the surrounding glowing meniscus — a raised melt surface connecting the crystal ingot with the flatter melt surface. Due to the intrinsic nature of the process, the bright ring radius measurement signal exhibits a non-minimum phase behaviour. A combination of the parallel compensator and a stabilizing controller is designed, such that the former provides for the mitigation of non-minimum phase behaviour, while the latter combined with the formal yields a suitable closed-loop performance.

Keywords: Czochralski process, bright ring radius measurement, parallel compensator, non-minimum phase, ray tracing, interface dynamics

1. INTRODUCTION

The CZ process is commercially used to grow monocrystalline crystals (silicon (Si), germanium, gallium arsenide), metal compounds and synthetic gemstones to name a few. Our study of the CZ process focuses on the growth of monocrystalline Si ingots. The growth process begins with the melting of silicon contained in a quartz crucible. The crucible receives heat input from the surrounding and base heaters. Then, a high purity Si seed crystal of the desired lattice structure is dipped into the melt, followed by pulling the seed gradually upwards such that the silicon solidifies at the seed crystal base, resulting in a cylindrical Si ingot.

The pulling mechanism comprises a pulling rod supported by a rotating metal shaft at the top, while the seed crystal is attached to the lower end of the pulling rod. The complete assembly of a commercial CZ puller is shown in Fig. 1. The pulling process causes a meniscus to form between the growing crystal ingot and the molten Si. Hence, the meniscus is a curved surface of the molten melt that protrudes above the flat melt level in the vicinity of the crystal ingot.

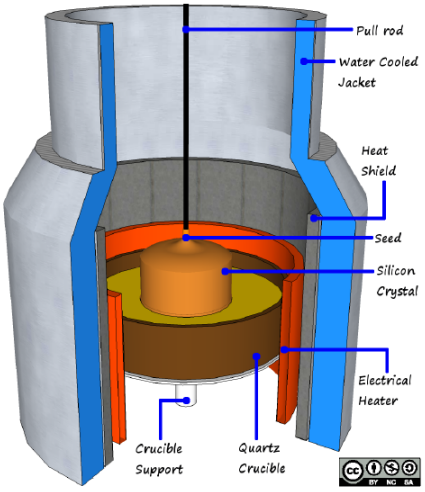

Fig. 1. Assembly of a typical CZ puller. (This figure is licensed under a Creative-Commons BY-NC-SA license) (Rahmanpour et al., 2017)

The accretion of crystal ingot continues as a result of heat loss from the top melt surface into a relatively colder environment. Although the crystal growth comprises of various stages, the commercial product is produced during the *body stage*, which is also the production stage addressed in this paper. During this stage, it is desired to maintain

⋆ The work is funded by the Norwegian Research Council's ASICO project 'project No. 256806/O20'

the crystal diameter constant which in turn depends on a balance between crystal growth and pulling speed.

Due to high temperatures inside the growth chamber, the light from the hot furnace components gets reflected by the meniscus. The reflected light appears as bright annular rings of varying intensities on the meniscus surface.

From a small viewing port at the pulling chamber, the crystal emerging from the meniscus can be visually inspected, though the crystal edge and the surrounding bright meniscus are indistinguishable. The high temperatures within the growth furnace prevent any direct measurement of the crystal radius. Instead, a pre-calibrated CCD camera aiming in the vicinity of the melt-crystal interface captures the image of the bright ring. Hence, the control of a simplified CZ crystal growth process boils down to bright ring radius measurement as a controlled variable, whereas pulling speed is a manipulated variable. During the entire growth process, the crucible is gradually lifted upwards to compensate for any changes in the melt level. Consequently, the position of the camera stays fixed.

In our previous work Bukhari et al. (2019), we investigated the anomaly in the bright-ring radius measurement by simulating the camera image through rigorous 3D ray-tracing simulation followed by the linearization of crystal growth dynamics based on the measurement model. The output of the linear models obtained, henceforth, exhibited the non-minimum phase behaviour. Such behaviour poses a fundamental limit on the achievable system bandwidth, thereby affecting the overall performance. This undesired effect of right-half-plane (RHP) zeros can neither be circumvented through simple feedback nor using series compensation. The latter results in pole-zero cancellation, which can pose problems related to the internal stability. However, based on parallel compensation, the location of RHP-zeros can be shifted. Therefore, as a sequel to our previous work, we continue to design a parallel compensator followed by a stabilizing controller in this paper.

2. PROCESS DYNAMICS

The complete description of the CZ process is highly complex and beyond the scope of the present work. Instead, we have considered basic growth dynamics at the interface Winkler et al. (2010) with two simplified heater models Bukhari et al. (2019).

2.1 Crystal Growth Dynamics

A simplified model for the crystal growth takes into account the process dynamics across the crystallization interface as depicted in Fig. 2. The model describes crystal radius r_c as a function of meniscus height h_c and crystal growth rate v_g, which in turn depends upon heat transfer balance across the crystallization (melt-crystal) interface. Thus, well-balanced heat/energy transfers ensure smooth and constant crystal growth. The simplified CZ model describing the crystal growth at the melt-crystal interface is given by:

$$\dot{r}_c = v_g \tan(\alpha_c) \tag{1a}$$

$$\dot{h}_c = v_p - v_g \tag{1b}$$

$$y = r_{br} \tag{1c}$$

where r_c is the crystal radius, h_c is the height of the meniscus at the three-phase boundary, v_g is the growth rate of the crystal (lengthwise) and v_p is the pulling speed. The measured output available for the feedback control is the bright ring radius r_{br}, estimated using a 3D ray-tracing simulation. The details of the estimation, based either on the numerical solution (Huh and Scriven, 1969) or the analytical approximation of the meniscus profile (Hurle, 1983), can be found in Bukhari et al. (2019).

The cone angle at the interface α_c is determined from the analytical approximation of meniscus height h_c given by Johansen (1994).

$$\alpha_c = \arcsin\left\{1 - \left(\frac{h_c}{a}\right)^2 \left[1 + 0.6915\left(\frac{r_c}{a}\right)^{-1.1}\right]\right\} - \alpha_0$$

where α_0 is the contact (*wetting*) angle at constant radius growth, while a is the capillary length. The overall growth angle α relates the cone angle α_c with the contact angle as $\alpha = \alpha_0 + \alpha_c$. In case of Si, the values of α_0 and a are 11° (Tatarchenko (1993), Rahmanpour et al. (2017)) and 7.62 mm, respectively.

The crystal growth rate is given as:

$$v_g = \frac{\phi_s - \phi_l}{\rho_s \Delta H} \tag{2}$$

where ϕ_s is the heat flux from the interface to the crystal, while ϕ_l is the heat flux from the meniscus to the interface. Two different models are used for describing the heat flux from the meniscus to the interface. **Model I** calculating the heat flux based on pure heat conduction across the meniscus, is given as:

$$\phi_{l,I} = \frac{k_{cond,I}}{h_c}(T_B - T_S) \tag{3}$$

In the second thermal model approach (**Model II**), the heat flux from the (melt + meniscus) to the interface is calculated on the basis of convective heat transfer as given in eq. (4)

$$\phi_{l,II} = h_{conv,II}\,(T_{bulk} - T_S) \tag{4}$$

where T_B is the temperature at the base of the meniscus, T_{bulk} is the temperature of the bulk of the melt and T_S is the temperature at the solidification interface, i.e., the melting temperature of Si.

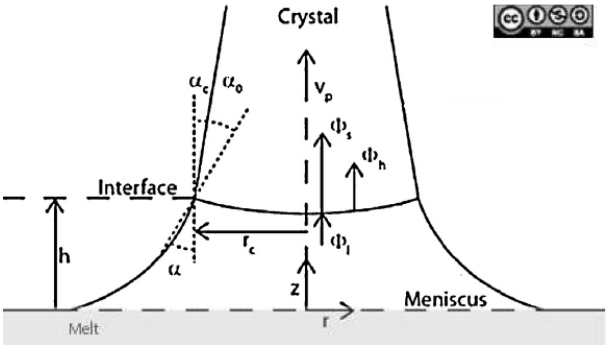

Fig. 2. Schematic view of the melt-crystal interface. (This figure is licensed under a Creative-Commons BY-NC-SA license) (Rahmanpour et al., 2017)

The measurement dynamics based on rigorous ray tracing method are explained in (Bukhari et al., 2019).

3. PLANT DYNAMICS AND CONTROLLER DESIGN

The linearized plant model, along with the 3D ray tracing measurement, possesses non-minimum phase characteristics due to the presence of a right-half plane zero (RHPZ) in the transfer function describing this dynamics.

Since the reader will frequently encounter the transfer function models henceforth, therefore in the upcoming text, the uppercase letters (e.g., $R_c(s)$) denote the Laplace transformed (frequency-domain) signals of their time domain counterparts (e.g., $r_c(t)$).

$G_p(s)$, the transfer function between $V_p(s)$ and $R_c(s)$, for the models I and II, is given in (5a) and (5b), respectively.

$$G_{p,I}(s) = \frac{-0.0047626}{(s - 8.78e^{-6})\,(s + 1.684e^{-3})} \tag{5a}$$

$$G_{p,II}(s) = \frac{-0.0048849}{(s - 4.63e^{-7})\,(s - 7.602e^{-6})} \tag{5b}$$

Similarly, the transfer functions between $R_c(s)$ and $R_{br}(s)$, i.e., $G_m(s)$, for the models I and II, are given in (6a) and (6b), respectively.

$$G_{m,I}(s) = -47.1864s + 1.0041 \tag{6a}$$

$$G_{m,II}(s) = -46.0050s + 1.0043 \tag{6b}$$

The measurement transfer functions in (6) are not physically realizable, unless multiplied by the corresponding transfer functions in (5) to obtain the overall transfer functions $G_I(s)$ and $G_{II}(s)$ for the models I and II, respectively. However, this factorization is quite handy when designing the parallel compensator in section (3.1). Fig. 3 shows the complete system block diagram that includes both the compensator and a stabilizing controller connected respectively in parallel and cascade with the plant.

The RHP zero in (6) cannot be relocated through feedback, as feedback can move the system poles only while the zeros stay unaffected. The parallel compensation, however, accomplishes the desired shift in RHP zero by making use of an additional branch in parallel to the main branch (cf. Fig. 3) comprising of the non-minimum phase system dynamics ((Skogestad and Postlethwaite, 2007)). The following sections will explain how to design such a parallel compensator to remove the bandwidth limiting effect of the RHP zero, thereby allowing fast feedback control and simplifying the design of stabilizing feedback.

3.1 Compensator Design

The non-minimum phase dynamics $G(s)$ combined with the parallel branch, comprising of compensator dynamics, result in the compensated system $G_{\tilde{r}}(s)$ that no longer possesses non-minimum phase characteristics.

The idea of using a parallel compensator to remove non-minimum phase characteristics is not new. However, in most cases, it does not make much sense, since the non-minimum phase dynamics are removed from the *compensated* measurement, and not from the physical measurement itself. Thus, while good control of the compensated measurement can be achieved, control of the physical measurement is still limited by the presence of the non-minimum phase dynamics. What makes the case of the Czochralski process stand out from the rest, is the fact, that the non-minimum phase dynamics are *not* associated with the variable desired to be controlled (the crystal radius), but rather with an indirect and inaccurate measurement thereof (the bright ring radius). It is, therefore, possible to make a compensated measurement, that is not just void of undesired non-minimum phase characteristics, but also serves a better approximation of the variable to be controlled.

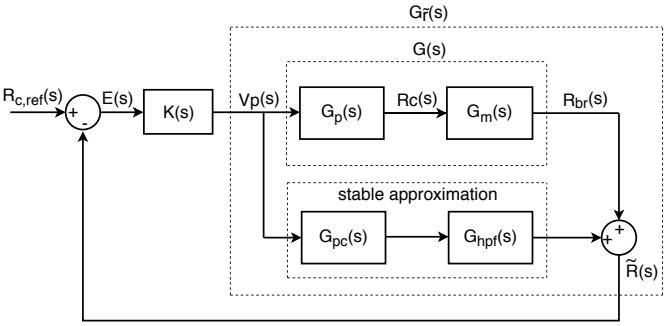

Fig. 3. Basic block diagram of plant with a parallel compensator

The compensator design procedure with reference to the proposed schematic, depicted in Fig. 3 is explained below: The parallel compensator $G_{pc}(s)$, (ignoring the high pass filter $G_{hpf}(s)$ for the time being) can be designed as:

$$\begin{aligned}\tilde{R}(s) &= \left[G_{pc}(s) + G_m(s)\,G_p(s)\right] V_p(s) \\ &= G_{\tilde{r}}(s)\,V_p(s)\end{aligned} \tag{7}$$

Ideally it is desired to have $\tilde{R} \approx R_c$. Therefore, the parallel compensator dynamics are given by:

$$G_{pc}(s) = \left[I - G_m(s)\right] G_p(s) \tag{8}$$

It is apparent from (7) and (8) that the ideal parallel compensator will contain the same unstable poles as those of the plant. Thus, having the identical unstable modes in the two parallel branches will lead to an unobservable (undetectable) compensated system. To avoid the compensator dynamics with any unstable modes from the plant, a stable approximation to the ideal (but unstable) parallel compensator is necessary.

For this purpose, a stable/unstable decomposition of the compensator dynamics is performed. The unstable mode spans the lower frequency range, and therefore, its dynamical contribution is reduced by connecting a high pass filter ($G_{hpf}(s)$) in cascade with the compensator. The stable/unstable decomposition is thus performed on the ideal precompensator with the high pass filter. The result is that the unstable part is very small, and is simply discarded.

An alternative to using the stable/unstable decomposition could be to use the Nehari extension (Zhou et al., 1996). Although it provides the best stable approximation to the unstable compensator dynamics, it does so by minimizing the absolute error and then distributing the error over all frequency ranges. The Nehari extension is not applicable in this work, because it shifts a significant amount of error from lower frequencies to higher frequencies, i.e.,

(the frequencies of interest). Thus, the 'stable/unstable decomposition' is a preferred approach for this work.

The designs of the parallel compensator and feedback controller are based on the model I, i.e., $G_I(s) = G_{p,I}(s)\,G_{m,I}(s)$, but verified using closed-loop simulation for both dynamic models I and II.

3.2 Controller Design

After the design of the parallel compensator, the design of a stabilizing feedback controller follows. The controller block marked as $K(s)$ in Fig. 3 is the automatic diameter controller (ADC), designed using PID control due to the ease, it offers towards the implementation in the existing industrial control setup. The PID controller is given by:

$$K(s) = \frac{K_p\,(T_i s + 1)\,(T_d s + 1)}{T_i s(1 + \frac{T_d s}{N})}$$

The tuned paraneters for the PID controller and the resulting cross over frequency are given in Table 1.

Table 1. PID Control Parameters

Proportional gain (K_p)	0.01 s ^{1}
Integral Time constt. (T_i)	5000 s
Derivative Time constt. (T_d)	650 s
Filter coefficient (N)	100
Crossover frequency (ω_{co})	0.032 75 rad s ^{1}

The achieved crossover frequency $\omega_{co} \approx 0.032\,75\,\mathrm{rad\,s^{-1}}$ shows that the limitations imposed by the RHP zero at $\approx 0.02\,\mathrm{rad\,s^{-1}}$ is quite clearly mitigated and a higher system bandwidth is achieved. The frequency response in Fig. 4 shows that the proposed PID controller with the compensator (based on **Model I**) stabilizes both models.

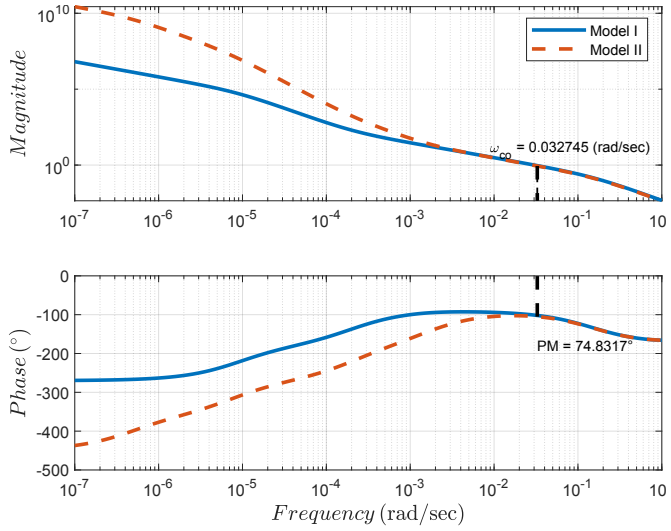

Fig. 4. Frequency response of the compensated plants (models I and II) with a feedback controller

4. CLOSED-LOOP PERFORMANCE

The closed-loop performance of the overall system, including both the compensator and the controller, designed on the basis of **Model I**, is evaluated for both model assumptions, i.e., **Model I & II** in (Bukhari et al., 2019) both linear and nonlinear environments.

The closed-loop responses (the bright ring radius measurement r_{br} and the compensated measurement $\tilde{r}$) of both linear plant models with a step change of 1 mm in commanded crystal radius $r_{c,ref}$ are shown in the top and the bottom panes of Figs. 5 and 6, respectively.

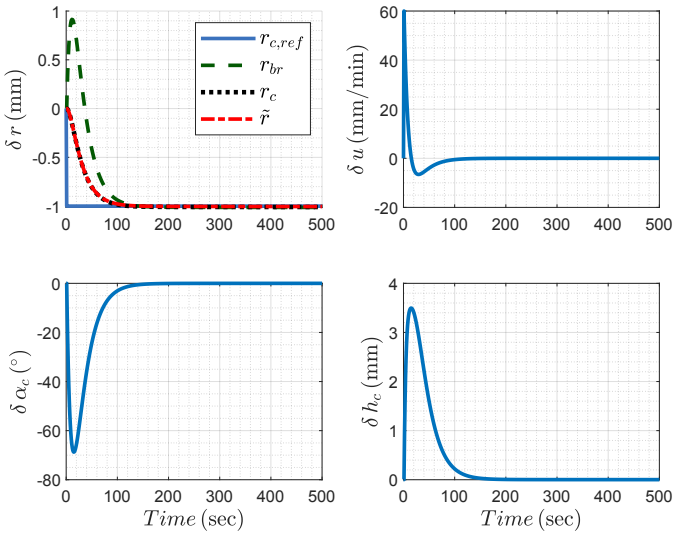

Fig. 5. Step responses for linear model I depicting changes in (bright ring radius measurement (r_{br}), crystal radius (r_c), compensated measurement ($\tilde{r}$)) (top-left pane) to a negative step change in ($r_{c,ref}$) alongwith the changes in control input (u) (top-right pane), crystal cone angle (α_c) (bottom-left pane) and meniscus height (h_c) (bottom-right pane)

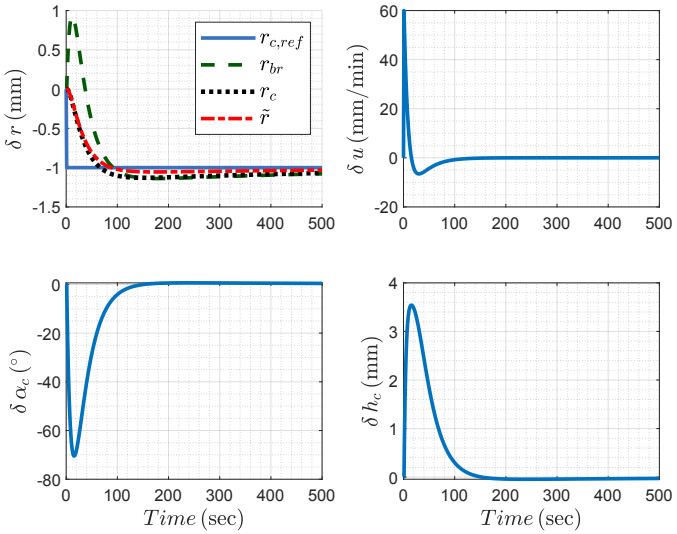

Fig. 6. Step responses for linear model II showing changes in (bright ring radius measurement (r_{br}), crystal radius (r_c), compensated measurement ($\tilde{r}$)) (top-left pane) to a negative step change in ($r_{c,ref}$) alongwith the changes in control input (u) (top-right pane), cone angle (α_c) (bottom-left pane) and meniscus height (h_c) (bottom-right pane)

In the case of **Model II** there is a small offset in both the bright ring radius measurement (r_{br}) and compensated

measurement ($\tilde{r}$) which is removed slowly. The closed-loop testing of nonlinear CZ growth dynamics in the presence of both parallel compensator as well as the feedback controller ($K(s)$) is illustrated in Fig. 7.

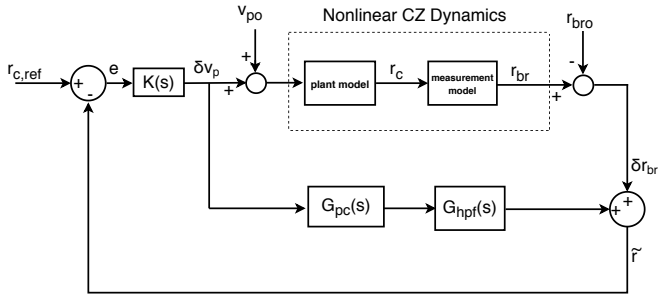

Fig. 7. Schematic for the closed-loop testing of nonlinear CZ growth dynamics

In Fig. 7, $\delta\, v_p$ and $\delta\, r_{br}$ are the deviation variables, whereas v_{po} and r_{bro} are the steady state values (points at which linearization was performed) such that the input to and the output from the nonlinear CZ dynamics are $v_p = v_{po} + \delta\, v_p$ and $r_{br} = r_{bro} + \delta\, r_{br}$, respectively.

Since, the real life physical systems are represented by variables that are smooth and uninterrupted, therefore the reference crystal radius trajectory is varied smoothly to analyze the resulting nonlinear closed-loop system responses. Figs. 8 and 9 depict the closed-loop performance, as the response of essential system parameters to a smooth, fast and negative crystal radius reference change for models I and II, respectively.

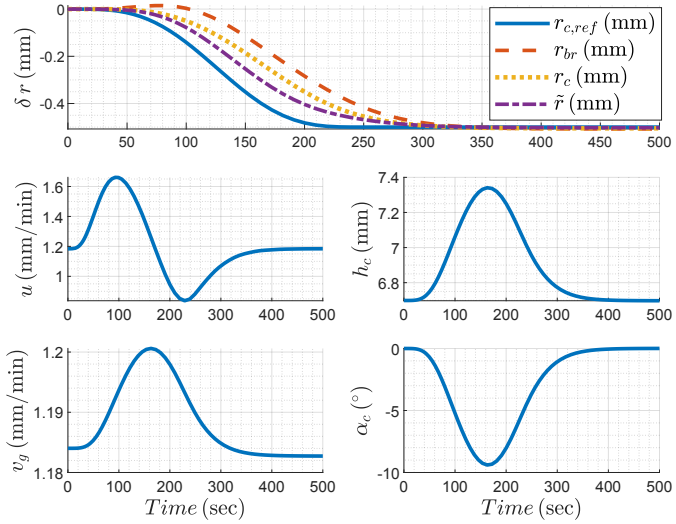

Fig. 8. Model I responses from a nonlinear CZ simulation (bright ring radius measurement ($\delta\, r_{br}$), crystal radius ($\delta\, r_c$), compensated measurement ($\delta\, \tilde{r}$)) (top pane) to a smooth and slow change in ($r_{c,ref}$) alongwith the control input (u) (middle-left pane), meniscus height (h_c) (middle-right pane), growth rate (v_g) (bottom-left pane) and cone angle (α_c) (bottom-right pane)

It is noteworthy that the first subfigure of Figs. 8 and 9 represent nonlinear quantities expressed in deviation variables. The change in reference trajectory amplitude is 0 mm to 0.5 mm taking place in 250 s.

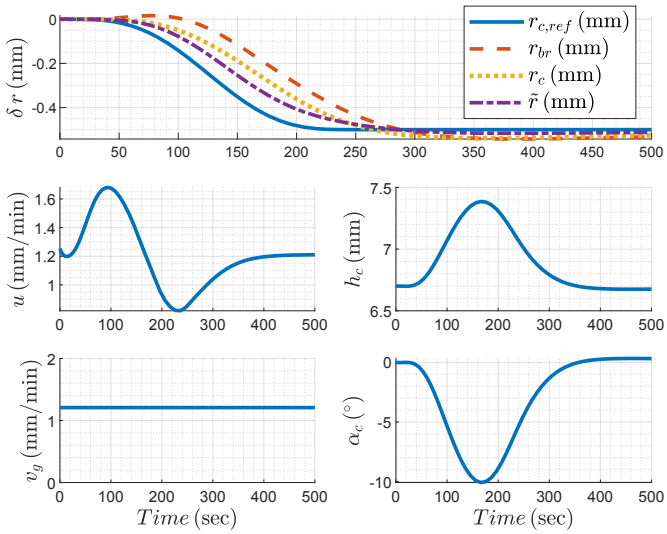

Fig. 9. Model II responses from a nonlinear CZ simulation (bright ring radius measurement ($\delta\, r_{br}$), crystal radius ($\delta\, r_c$), compensated measurement ($\delta\, \tilde{r}$)) (top pane) to a smooth and slow change in ($r_{c,ref}$) alongwith the control input (u) (middle-left pane), meniscus height (h_c) (middle-right pane), growth rate (v_g) (bottom-left pane) and cone angle (α_c) (bottom-right pane)

5. CONCLUSIONS

The bright-ring radius measurement used as a controlled variable in the CZ process possesses an RHP zero that limits the achievable system bandwidth and hence the overall system performance. This nonminimum phase behaviour is dispensed with the use of parallel compensation, thereby enabling the use of a feedback controller, which in turn, provides improved performance of the system. Moreover, the compensated plant stabilized through a PID controller performs satisfactorily for both thermal model assumptions.

Future work will study how the temperature-induced disturbances entering the crystalization interface affect the overall crystal radius control regime.

REFERENCES

Bukhari, H.Z., Hovd, M., and Winkler, J. (2019). Limitations on control performance in the Czochralski crystal growth process using bright ring measurement as a controlled variable. *IFAC-PapersOnLine*, 52(14), 129–134.

Huh, C. and Scriven, L. (1969). Shapes of axisymmetric fluid interfaces of unbounded extent. *Journal of Colloid and Interface Science*, 30(3), 323–337.

Hurle, D. (1983). Analytical representation of the shape of the meniscus in Czochralski growth. *Journal of Crystal Growth*, 63(1), 13–17.

Johansen, T.H. (1994). An improved analytical expression for the meniscus height in Czochralski growth. *Journal of Crystal Growth*, 141(3-4), 484–486.

Rahmanpour, P., Sælid, S., and Hovd, M. (2017). Run-to-run control of the Czochralski process. *Computers & Chemical Engineering*, 104, 353–365.

Skogestad, S. and Postlethwaite, I. (2007). *Multivariable Feedback Control: Analysis and Design*, volume 2. Wiley New York.

Tatarchenko, V. (1993). *Shaped Crystal Growth*, volume 20. Springer Science & Business Media.

Winkler, J., Neubert, M., Rudolph, J., Duanmu, N., and Gevelber, M. (2010). Chapter 3, Czochralski Process Dynamics and Control Design. In *Crystal Growth Processes Based on Capillarity: Czochralski, Floating Zone, Shaping and Crucible Techniques*, 115–202. John Wiley & Sons, Ltd.

Zhou, K., Doyle, J.C., and Glover, K. (1996). *Robust and Optimal Control*, volume 40. Prentice-Hall, Upper Saddle River, NJ, USA.